The Astrophysical Journal, 788:145 (14pp), 2014 June 20 doi:10.1088/0004-637X/788/2/145

CIRCUMNUCLEAR MOLECULAR GAS IN MEGAMASER DISK GALAXIES NGC 4388 AND NGC 1194

Jenny E. Greene[1], Anil Seth[2], Mariya Lyubenova[3], Jonelle Walsh[4], Glenn van de Ven[3], and Ronald Läsker[3]
[1] Department of Astrophysics, Princeton University, Princeton, NJ 08540, USA
[2] University of Utah, Salt Lake City, UT 84112, USA
[3] Max Planck Institute for Astronomy, Königstuhl 17, D-69117 Heidelberg, Germany
[4] Department of Astronomy, The University of Texas at Austin, 2515 Speedway, Stop C1400, Austin, TX 78712-1205, USA
Received 2014 February 3; accepted 2014 April 29; published 2014 June 3

ABSTRACT

We explore the warm molecular and ionized gas in the centers of two megamaser disk galaxies using K-band spectroscopy. Our ultimate goal is to determine how gas is funneled onto the accretion disk, here traced by megamaser spots on sub-parsec scales. We present NIR IFU data with a resolution of ∼50 pc for two galaxies: NGC 4388 with VLT/SINFONI and NGC 1194 with Keck/OSIRIS+AO. The high spatial resolution and rich spectral diagnostics allow us to study both the stellar and gas kinematics as well as gas excitation on scales only an order of magnitude larger than the maser disk. We find a drop in the stellar velocity dispersion in the inner ∼100 pc of NGC 4388, a common signature of a dynamically cold central component seen in many active nuclei. We also see evidence for noncircular gas motions in the molecular hydrogen on similar scales, with the gas kinematics on 100 parsec scales aligned with the megamaser disk. In contrast, the high ionization lines and Brγ trace outflow along the 100 parsec-scale jet. In NGC 1194, the continuum from the accreting black hole is very strong, making it difficult to measure robust two-dimensional kinematics, but the spatial distribution and line ratios of the molecular hydrogen and Brγ have consistent properties between the two galaxies.

Key words: galaxies: ISM – galaxies: nuclei – galaxies: Seyfert

Online-only material: color figures

1. INTRODUCTION

Active galactic nuclei pose a fundamental problem—how does rotationally dominated gas on kiloparsec scales lose orders of magnitude in angular momentum to fall onto an accretion disk on AU scales (e.g., Balick & Heckman 1982). We do not know the mechanism that dissipates angular momentum and allows gas to accrete. There is no shortage of ideas, including major or minor mergers (e.g., Dahari 1985; Mihos & Hernquist 1994; Kuo et al. 2008; Ellison et al. 2011), bars and bars within bars (e.g., Shlosman et al. 1990; Maciejewski et al. 2002; Hunt et al. 2008; Kim et al. 2012), and nuclear spirals (Englmaier & Shlosman 2000; Maciejewski 2004; Martini et al. 2003; Ann & Thakur 2005) as perhaps indicated by dust lanes (Simões Lopes et al. 2007; Martini et al. 2013). Even looking directly at molecular gas kinematics on parsec scales in active galaxies, it is very hard to find clear evidence for the true driver of nuclear activity (Haan et al. 2009; García-Burillo et al. 2009; García-Burillo & Combes 2012; Combes et al. 2014).

Due to the advent of near-infrared integral-field spectrographs (NIR IFU hereafter), there has been significant progress in understanding gas flows in the centers of active galactic nuclei (AGNs) in recent years. The NIR observations allow us to penetrate gas and dust in the active nuclei, and, in conjunction with adaptive optics, to probe very near to the nucleus. In some nearby cases, inflows are directly observed along circumnuclear spirals in ionized gas on ∼100 pc scales (e.g., Storchi-Bergmann et al. 2007; Davies et al. 2009; van de Ven & Fathi 2010; Riffel et al. 2013b). Furthermore, there are intriguing hints of kinematic differences in the nuclei of local Seyfert galaxies. For example, Dumas et al. (2007) suggest that the ionized gas in the disks of Seyfert galaxies (i.e., outside of the narrow-line region or NLR) is more kinematically disturbed than the gas in a control inactive sample. Hicks et al. (2013) also report that Seyfert galaxies have more concentrated stellar luminosity profiles, lower stellar velocity dispersions, and elevated H_2 1–0 $S(1)$ emission within ∼100–200 pc relative to an inactive subsample.

In this work, we specifically focus on megamaser disk galaxies. In these special systems, luminous water megamasers at 22 GHz trace a geometrically thin molecular disk on sub-parsec scales in orbit around the central black hole (BH; e.g., Miyoshi et al. 1995; Herrnstein et al. 2005; Lo 2005; Kuo et al. 2011). The megamaser spots show near perfect Keplerian rotation in many (e.g., Kuo et al. 2011), but not all cases (e.g., Lodato & Bertin 2003; Kondratko et al. 2005). Due to the Keplerian rotation in the maser disk, we know the BH mass to a few percent, limited in most cases by the distance to the galaxy (e.g., Kuo et al. 2011). Direct geometric distances have also been derived by measuring the accelerations of the systemic masers for the few best cases (Herrnstein et al. 2005; Reid et al. 2009, 2013; Kuo et al. 2013).

In addition to distance measurements and BH masses, the megamaser disk reveals the spin axis of the accretion disk on sub-parsec scales. To get the long path lengths required for masing, the disk must be virtually edge-on; we thus typically know the orientation of the disk on sub-parsec scales to within a couple of degrees (Kuo et al. 2011). We have already found that the spin axis of the megamaser disk aligns with the jet on ∼100 pc scales, while the spin axis of the disk does not appear to align with flattened disk-like structures on ∼500 pc scales identified in *HST* imaging (Greene et al. 2013). In this paper, we explore the use of NIR IFU data to define the gas flows on $\lesssim$500 pc scales, for comparison with the megamaser disk. We currently have NIR IFU observations of the centers of two galaxies in the Kuo et al. sample: NGC 4388 and NGC 1194. These two are the only two megamaser disk galaxies with published BH masses where we can come close to resolving the gravitational sphere of influence, in the former case because the galaxy is nearby (in Virgo) and in the latter because the

BH is the most massive known with a maser disk (Kuo et al. 2011).

2. OBSERVATIONS AND DATA REDUCTION

2.1. NGC 4388 with SINFONI

We observed NGC 4388 with SINFONI under program 386.B-0244A[5] on the Very Large Telescope (Eisenhauer et al. 2003; Bonnet et al. 2004) on 2011 April 12 and May 5 in natural seeing conditions and in service mode. We have been awarded time to observe this galaxy at two spatial resolutions, the higher one involving the assistance of the Adaptive Optics system (AO), however, to date these observations are only partially carried out. Thus, in this paper, we present the lower spatial resolution data set that covers a wider field of view.

Our observations cover the central $8'' \times 8''$, with a spatial sampling of $0''.125 \times 0''.250$. We used the *K*-band grating (1.95–2.45 μm) that gives a spectral resolution $R \sim 3500$ (6.2 Å FWHM, as measured on sky lines). For the observations we used standard near-IR nodding techniques. Observing blocks consisted of a sequence of object and sky frames (OSOOSOOSOOSOO). Each individual integration was 300 sec and the sky fields were offset by $240''$ to the North and East. Science frames were dithered by $0''.3$ in order to reject bad pixels. There were two observing blocks, with a total on-source integration time of 100 minutes, and 40 minutes in total on sky frames. Additionally, after each observing block and at a similar airmass, we observed a B dwarf star to act as a telluric star.

We used the ESO SINFONI pipeline v2.3.3 to perform the basic data reduction on each observing block, consisting of 10 object and 4 sky exposures. In brief, the pipeline extracts the raw data, applies distortion, bad pixel and flat-field corrections and wavelength calibration, and stores the combined sky-subtracted spectra from one observing block in a three-dimensional data cube. The final pixel size is $0''.125$.

We reduced the telluric stars in the same way as the science frames. For each telluric star we extracted a one-dimensional spectrum, removed the hydrogen Brackett γ absorption line at 2.166 μm after fitting it with a Lorentzian profile, and divided the star spectrum by a black body spectrum with the same temperature as the star. The last step in preparing the telluric spectrum was to apply small shifts in the spectral direction (<0.05 pixels or 0.123 Å) and scalings to minimize the residuals of the telluric features. To do this, we extracted a central one-dimensional spectrum from each science data cube and cross-correlated and fitted it with the corresponding telluric spectrum. We derived the wavelength-dependent correction required to match the continuum shape of the telluric star (without an absolute zero-point). Thus, when we divided each individual spaxel in the six galaxy data cubes by the corresponding best-fitting telluric spectrum, we also obtained a relative flux calibration.

Based on the seeing monitor, during our observations the seeing varied from 1 to $1''.5$ for the first observation, and between 0.5 and $0''.7$ for the second observation. Note that the seeing monitor takes measurements at 5000 Å, thus our seeing is typically better than this. From the standard stars (taken at the end) we measure a FWHM of $0''.8$ for the first observation and $0''.5$ for the second. We aligned the two OBs with integer offsets and summed them; all analysis was done on this final summed data cube.

2.2. NGC 1194 with OSIRIS

We observed NGC 1194 using the IFU OH-Suppressing Infrared Imaging Spectrograph (OSIRIS Larkin et al. 2006) assisted by the laser-guide star adaptive optics system (Wizinowich et al. 2006; van Dam et al. 2006) on the 10 m Keck II telescope. The data were taken over the latter two-thirds of a single night on 2011 October 19. We observed in the *K* band with the Kbb filter, for a spectral coverage of 1.965–2.381 μm and a spectral resolution of $R \approx 4000$. We used the $0''.05$ spatial scale, and oriented the long axis of the IFU along the major axis of the galaxy at a P.A. of 145°. We dithered the galaxy by $0''.2$ perpendicular to the long axis of the IFU, both to facilitate bad pixel removal and to slightly increase the field of view to $1''.2 \times 3''.2$.

Unfortunately, the nucleus of NGC 1194 was too faint to use as a tip-tilt star. Thus, we used a nearby ($54''$) star (ID = 0888-0029937; $R = 14.7$). Natural seeing conditions varied over the night from $0''.5$ to $1''.1$. From our final science data cube we find that the PSF core had a FWHM of $0''.16$ as measured from the galaxy core. We also observed a telluric standard (A0V) star approximately once per unit change in airmass. Finally, we interleaved sky and object observations with an Object-Sky-Object pattern, spending 600s per sky and object exposure. We acquired a total of 170 min on source.

We followed closely the reductions outlined in Walsh et al. (2012), using the OSIRIS data reduction pipeline (v2.3) made available by the instrument team.[6] We repeat salient details here for completeness. The pipeline handles sky subtraction, cosmic-ray removal, glitch identification, spectral extraction into a data cube, wavelength calibration, atmospheric dispersion correction, and telluric correction using an A0V star. We experimented with a scaled sky subtraction method from Davies (2007), but did not find substantial improvements from the direct method. Finally, we determined the centroid of each exposure by hand, applied these sub-pixel offsets, and averaged all cubes into our final data cube.

3. SPECTRAL ANALYSIS

Here we describe our analysis procedure for the NGC 4388-SINFONI data cube in detail, highlighting any differences in analysis with the NGC 1194 data cube.

3.1. Stellar Kinematics

We use the direct-pixel-fitting code pPXF of (Cappellari & Emsellem 2004) to fit the stellar continuum. To achieve an adequate signal-to-noise ratio (S/N), we use the Voronoi binning scheme of Cappellari & Copin (2003), which determines contiguous bins with uniform S/N, in this case S/N > 50 per pixel. The SINFONI pipeline does not return an error array, and so the noise is determined empirically from line-free regions of the spectrum as the variance in the spectrum once large outliers are clipped. In the case of the OSIRIS data, we use the per-pixel error array generated by the reduction pipeline. We then fit the coadded spectrum corresponding to each bin with a weighted combination of stellar templates. Each template is shifted to the systemic velocity of the galaxy and convolved with a Gaussian line-broadening function. A polynomial of fourth order is added to account for nonthermal continuum from the AGNs, and

[5] We are grateful to the ESO astronomers who obtained the data presented in this paper in service mode operations at La Silla Paranal Observatory.

[6] http://irlab.astro.ucla.edu/osiris/pipeline.html

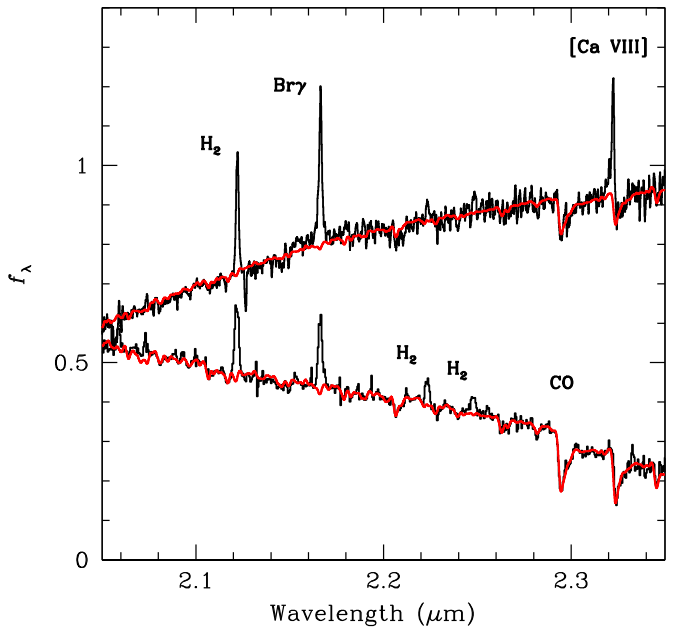

Figure 1. Example fits to the stellar continuum of NGC 4388 using pPXF and stellar templates observed with SINFONI. The top spectrum is the sum of pixels within the AGN-dominated central point source, showing the strong nonthermal AGN continuum. The bottom spectrum represents the sum of all high S/N pixels from the galaxy disk excluding the central point source, which we fitted to derive a best-fit average template, as described in Section 4.1. The relatively blue spectrum here is dominated by stellar light. Due to telluric residuals, we truncate the spectra at the blue end for display purposes.

(A color version of this figure is available in the online journal.)

potentially flux calibration errors as well. Example fits are shown in Figure 1.

The measurement uncertainties in both velocity and velocity dispersion are determined with Monte Carlo simulations. In the case of the NGC 1194 data, the data reduction software generates an error array. However, for the NGC 4388 data, we use residuals from the best fit (with the emission lines removed) to determine the average sigma. We create 100 perturbed input spectra assuming Gaussian errors in the spectra. We then refit these 100 artificial spectra. The uncertainty in each parameter is calculated as the values encompassing 68% of the trials.

We experimented with a number of fitting regions, including a fit to the bandhead only (2.2–2.4 μm, short), a fit to the full region (1.95–2.4 μm, full), and an intermediate region (2.04–2.4 μm, best). We found that the first fit delivered reliable velocity dispersions, but unstable radial velocities because of the narrow wavelength range, and because the bandhead at 2.32 μm is often filled in by [Ca VIII] λ2.322 μm emission. Fits to the full spectral region suffered from telluric residuals at $\sim$2 μm. The just-right spectral region was therefore the third, intermediate case. The median errors on the velocities are 7, 12, 9.5 km s^{-1} for the best, short, and full regions, respectively, while the median errors on the dispersion measurements are 8.5, 8.5, 12 km s^{-1}. In all cases, we masked high-EW emission lines, including the H_2 lines at 2.034, 2.042, 2.066, 2.073, 2.122, 2.154, 2.201, 2.211, 2.223 , 2.248, 2.254, 2.287, 2.345 μm and also [Si VI] λ1.963 μm, He I λ2.059 μm, Brγ λ2.166 μm, and [Ca VIII].

To bracket uncertainties caused by template mismatch, we utilize two stellar template libraries in fitting the SINFONI data. One is a library of stars observed with SINFONI using the same observational set-up. In this case, no correction for instrumental resolution is required. The native SINFONI templates range from K4III to M5III (plus a K4.5V star) (Lyubenova et al. 2008). As a check, we also use the stellar template library of Wallace & Hinkle (1996), observed at higher spectral resolution. We use this second template set only to test our sensitivity to template mismatch. The Wallace templates cover a wider range in spectral type, including KM supergiants and KM giants. We discuss the stellar template fits to the NGC 4388 data in detail in Section 4.1.

Even with different templates, we find good agreement in the two sets of stellar velocity dispersion measurements. Taking σ_S as the answer based on the SINFONI templates and σ_W as the same for the Wallace templates, we find $\langle(\sigma_S - \sigma_W)/\sigma_S\rangle = -0.05 \pm 0.2$ (where the latter number is simply the standard deviation in this ratio). We find that the two measurements agree within 20% (i.e., within the observational uncertainties) and we find no significant systematic offset. In the case of the OSIRIS data, our primary fitting uses a single K5III star, which provides an acceptable fit to our moderate S/N data.

3.2. Finding the Center

We do not a priori know the location of the BH, or the precise photometric center of the galaxy. We could use the continuum to determine the photometric center, but then we would be sensitive to obscuration, which is still significant in the NIR (see Figure 2). Instead, we use the equivalent width of the CO bandhead to determine where the active nucleus peaks (Davies et al. 2004, 2007). We use the index definition from Oliva et al. (1995): the index band is 2.2924–2.2977 μm, with a continuum band centered on 2.2900 and a width of 0.0003 μm, and we also followed their prescription to correct for velocity dispersion although this correction is negligible (see also Förster Schreiber 2000). These authors show that in the absence of an active nucleus, star-forming galaxies have a very uniform CO EW. A declining CO EW towards the galaxy center can be attributed to infill by the nonthermal continuum from the accreting BH. We show an example in Section 4.1.

We create an AGN continuum map by taking the CO EW at the edge of the cube (EW = 9.5 Å in NGC 4388, consistent with stellar-population models) and assuming that all dilution further inwards results from the AGNs, such that continuum (AGN) = [total continuum] $\times$ [1 - CO EW/CO Outer]. The photometric center of the continuum map falls 0.″0875 South of the CO EW center. The optical narrow-line region cone is only visible to the South (Section 4.2.3), so it is sensible that the continuum centroid should be shifted towards the low-reddening side of the disk. The best-fit center also agrees within less than a pixel with the peak H_2 and Brγ emission, although these latter are not as well defined. We will use this position as the center of the cube throughout. In the case of NGC 1194, the CO-derived and photo-centers agree within <0.″005.

3.3. Emission Line Fitting

While Voronoi binning is very useful to create uniform continuum S/N (e.g., Cid Fernandes et al. 2013), it is more difficult to apply to patchy emission-line maps, where by using large bins we may smear out interesting features in the line emission maps. We therefore create a second data cube using a 3 $\times$ 3 pixel smoothing in the outer regions and a 2 $\times$ 2 pixel binning in the inner 2 $\times$ 2″ region. With this level of binning, we increase the S/N by a factor of two but still maintain multiple pixels across the PSF. We measure the emission lines from this uniformly gridded cube. In the case of NGC 4388, because we have such high S/N in the continuum, we again perform

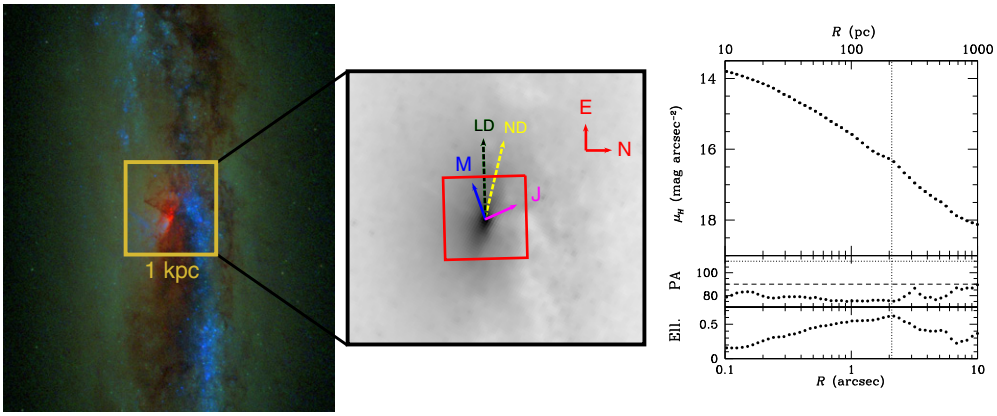

Figure 2. Left: three-band *HST*/WFC3 image including filters F336W, F438W, and F814W (Greene et al. 2013). To match the data cube, E is up and N to the right, identical to the middle image. The yellow box has a size of 11″ (∼1 kpc), and matches the region shown in the middle image. Middle: a zoom-in on the nuclear disk as revealed by our *HST*/WFC3 F160W image. The red box shows a 4 × 4″ region (360×360 pc), corresponding to the SINFONI IFU region that we display in all subsequent figures. We schematically indicate the 24° orientation of the 100 parsec-scale jet (J; magenta), the maser at 107° (M; blue), the large-scale disk at 90° (LD; black dashed), and the nuclear disk at 75° (ND; yellow dashed). Right: radial profile of the F160W image, including P.A. measured E of N, and ellipticity. The extent of the nuclear disk, with a P.A. of 75°, is indicated with the vertical dotted lines. We also indicate with horizontal lines the P.A. of the large-scale disk (90°, dashed) and the megamaser disk on sub-parsec scales (107°, dotted).

(A color version of this figure is available in the online journal.)

continuum-subtraction using pPXF before fitting the emission lines. However, there are no strong stellar absorption features beneath the emission lines of interest, and thus for NGC 1194, where the S/N is poor in the continuum, we simply fit a local continuum value.

We fit each emission line independently. We model the intrinsic line shape as a Gaussian, although we allow for up to two Gaussian components for emission lines with S/N > 4 in NGC 4388. Particularly in the Brγ and [Si VI] lines, the line shapes are often non-Gaussian and warrant a second component. In ∼50–60% of cases within the central 2 × 2″, the S/N is sufficient to warrant a two-component fit. We calculate the non-parametric FWHM from the sum of Gaussian components, and from that value a corresponding line dispersion. We also experimented with an empirically determined line-broadening function by fitting a Gauss–Hermite model to the strong sky emission lines, which caused only very minor changes in our fits. We derive errors on all the fitted parameters by fitting 100 artificial spectra that are created as a sum of the original spectrum and a Gaussian random noise array generated from the extracted errors.

4. NGC 4388

NGC 4388 is an SBb galaxy at a distance of 19 Mpc (Kuo et al. 2011), corresponding to a physical resolution of ∼50 pc given our ∼0.″5 seeing. The galaxy magnitude is $M_r = -20.1$ mag, with a $B/T \sim 0.5$ based on fits to the SDSS data (Greene et al. 2010). We show an *HST*/WFC3 image combining F336W (broad *U*), F435W (broad *B*), and F814W (broad *I*) in Figure 2. With a photometric P.A. of 90°, the galaxy is very nearly edge-on, which is not true for the majority of the megamaser disk galaxies (Braatz et al. 1997; Greenhill et al. 2009). The inclination determined from the large-scale kinematics is 78° (Veilleux et al. 1999a), and the systemic velocity from the same study is $v_{\rm sys} = 2525 \pm 25$ km s^{-1}. The gas kinematics show an isophotal twist on arcmin scales, which Veilleux et al. (1999a) successfully model as a bar within the inner 1.5 kpc, with a P.A. of 100° on the sky. The bar is also apparent in the photometry as a boxy bulge.

NGC 4388 is well known as a galaxy that is falling into the Virgo cluster (Yasuda et al. 1997). Gas is being stripped from the galaxy, as evidenced by an H I and ionized gas tail (Ford et al. 1971; Phillips & Malin 1982; Pogge 1988; Corbin et al. 1988; Petitjean & Durret 1993; Veilleux et al. 1999b; Stoklasová et al. 2009). There is even a detection of the photoionized gas in the soft X-rays (Iwasawa et al. 2003).

We are interested in the center of NGC 4388, in particular because of the megamaser disk on sub-parsec scales (Braatz et al. 2004). Based on the megamaser rotation curve, the BH mass is found to be $8.4 \pm 0.9 \times 10^6\ M_\odot$ (Kuo et al. 2011). Combined with the bolometric luminosity estimate from Vasudevan et al. (2013), the Eddington ratio is $L_{\rm bol}/L_{\rm Edd} \approx 10\%$, which is in very rough agreement with our estimate from the [O III] luminosity (Greene et al. 2010). Like most megamaser disk galaxies (Greenhill et al. 2008), the AGN in NGC 4388 is Compton thick and quite bright in hard X-rays (e.g., Hanson et al. 1990; Takano & Koyama 1991; Iwasawa et al. 1997; Forster et al. 1999; Fedorova et al. 2011). NGC 4388 has also been seen to change state in the X-ray (Elvis et al. 2004), switching from being Compton thick to Compton thin. Weak broad Hα has also been reported at the galaxy center (Filippenko & Sargent 1985; Ho et al. 1997).

4.1. Stellar Kinematics

We first examine stellar rotation and dispersion. We clearly see rotation within our ∼300 pc field of view that aligns with the disk on larger scales. Following Cappellari et al. (2009), we first use pPXF to fit the average spectrum over all data, excluding a 0.″5 radius around the AGN (Figure 1). In the fiducial fits, we do not fit higher-order Gauss–Hermite moments. We will examine h3 and h4 in Section 4.1.1 below. All of our default fits employ the SINFONI templates. From this high S/N spectrum we can derive the best-fit spectral mix, which may be degenerate in lower S/N individual spectra. Based on our fit to this average spectrum, we find a dispersion of 105 ± 7 km s^{-1}, which compares well with our previous measurement of 107 ± 7 km s^{-1} (Ho et al. 2009; Greene et al. 2010). The best-fit template is composed of 50% K4/5III, 38% K7III, and 12% M5 II/III stars.

We then fit spatially resolved spectra across the cube, using Voronoi binning to ensure comparable S/N in all bins. We both allow the mix of templates to be a free parameter, and use

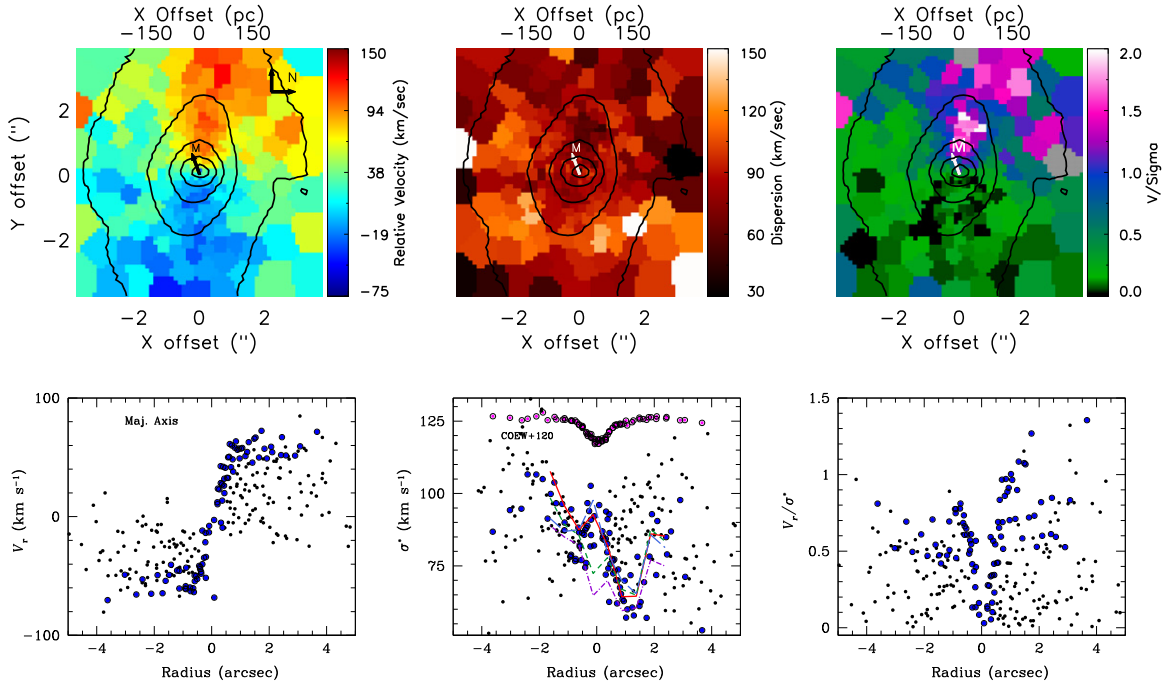

Figure 3. Top: stellar rotation (left), velocity dispersion (center), and V/σ (right) fields as derived from the Voronoi-binned data using pPXF. The orientation has north left and east up, while the sub-parsec megamaser disk orientation is indicated. Bottom: rotation (left), velocity dispersion (center), and V/σ (right) as a function of radius at all position angles (black) and along the major axis (blue). For illustration (center), we also show the CO EW along the major axis slice in magenta, scaled up for plotting purposes. Particularly note the asymmetric fall in dispersion seen only to one side of the galaxy. To investigate whether this drop in σ_* is real, or an artifact of the fitting, we refit with a polynomial degree of two (red solid line), only K5III templates (green dashed line) and with Wallace templates using only giant stars (long-dashed royal blue). Although the dispersion in the center is uncertain due to AGN contamination, the σ-drop persists in all of these fits.

(A color version of this figure is available in the online journal.)

the best-fit mixture from the high S/N fit to the entire cube. The latter fit has the advantage that by decreasing the number of free parameters, we increase the fitting stability in the AGN-dominated region (Cappellari et al. 2009). However, we find excellent agreement between the two measurements, with the scatter in their fractional difference being only 9%. Thus, we will present results with the stellar templates allowed to vary.

The fitted rotation and dispersion fields are shown in Figure 3. Our best-fit systemic velocity is 2530 km s^{-1}, consistent with the measurement of Veilleux et al. (1999a). We do find a systematic difference of ∼20 km s^{-1} between the absolute velocity derived when we use the SINFONI stellar templates and that from the Wallace et al. templates. We are not sure of the origin of this difference; it is possible that the SINFONI template stars, while all at rest relative to each other, have not been shifted to a rest velocity. We thus quote an uncertainty of 2530 ± 20 km s^{-1} in the systemic velocity.

4.1.1. Stellar Rotation Curve

To derive the rotation curve, we use the *kinemetry* formalism of Krajnović et al. (2006), which is similar to ellipse fitting of photometry, but operates on both even and odd moments of the kinematic field. The kinematics are modeled using a sixth order expansion along ellipses with the position angle and ellipticity as free parameters. We show the resulting rotation curve in Figure 4, along with the best-fit ellipse P.A., ellipticity ϵ, and the amplitudes of the higher-order terms that encapsulate deviations from simple circular rotation.

We clearly measure rotation in the stellar kinematics, with a maximum amplitude of $V_{\rm max} \approx 60$ km s^{-1}. The stellar rotation axis of 90° is aligned with the major axis of the kiloparsec-scale disk. On larger scales, Stoklasová et al. (2009) measure a stellar rotation of 60–80 km s^{-1} out to ∼4″ (∼300 pc), consistent with ours, which then appears to fall slightly at larger radius.

With $\sigma_* \approx 110$ km s^{-1} beyond 1″(100 pc), we find a $V/\sigma \approx 0.6$. Overall, the stars are dispersion-dominated, but we see signs of kinematic components apart from just a bulge. First, for a $V/\sigma \approx 0.6$, we would expect an ellipticity of $\epsilon < 0.3$ for an isotropic oblate rotator (Binney 1978), rather than the $\epsilon \approx 0.5$–0.6 that we observe in the isophotes (Figure 2). Second, within a radius of ∼1.″5 the dispersion field actually drops (although the decrement is more pronounced on the east side of the disk). On the same scale, we see a jump in velocity, P.A., and ellipticity likely signaling a transition from an inner disk to more bulge-dominated kinematics. Third, we also detect a disk-like structure in the inner 100 pc in the *HST*/WFC3 F160W image (Figure 2). The nuclear disk appears to have P.A. ≈ 75°, misaligned with the large-scale disk, and a size very similar to the σ-drop region. We detect this same disk component in more detailed two-dimensional fitting of the *HST*+ground-based data (R. Läsker et al. 2014, in preparation).

The most likely explanation of these observations is that there is a disk within 2″ (180 pc) embedded in the larger-scale bulge/bar. Only on unextincted sight lines are the kinematics dominated by the disk component, while on heavily extincted sight lines we are seeing the kinematics in the bulge/bar. The falling rotation curve outside 400 pc may also reflect the increasing dominance of the bulge/bar on larger scales. As additional confirmation of this picture, we refit the stellar kinematics and measure the higher-order Gauss–Hermite moments h3 and h4 (e.g., van der Marel & Franx 1993). Although individual h3 measurements have only S/N ≈ 0.5–2, we do find the classic anti-correlation between h3 and V/σ that points to the superposition of a bulge and disk, as seen both in simulations

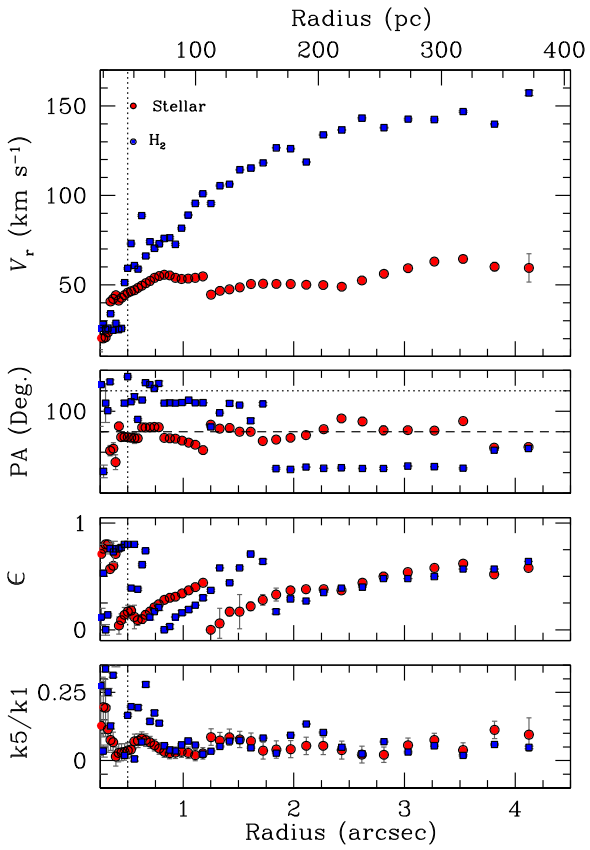

Figure 4. Properties of the velocity maps as derived from kinemetry (Krajnović et al. 2006) from both the stars (red circles) and the H_2 2.12 μm gas (blue squares). We show, in order from top to bottom, the rotation curve, the position angle (measured east of north), the ellipticity ϵ, and the higher-order deviations from a circular velocity pattern. Our kinematic P.A. is consistent with previous measurements. For reference, we also show the P.A. of the large-scale disk (90°) and of the megamaser disk (107°). We see that most of the interesting deviations occur within the inner ∼2″ (200 pc). The gas is considerably colder than the stars, with a rotation amplitude of 150 vs. 60 km s^{-1}, respectively.

(A color version of this figure is available in the online journal.)

(Hoffman et al. 2009) and data (e.g., Bender et al. 1994; Krajnović et al. 2008; Seth 2010). We also find two additional hints that the K-band extinction is higher to the West. First, we find a significantly redder continuum slope to the West side of the disk, corresponding to a differential $A_V \approx 2$ mag assuming a Cardelli et al. (1989) reddening law. Second, we clearly see a dip in the H_2 emission on the same scale on the west side of the disk (see Section 4.2).

Next, we will ensure that the σ-drop is real and not an artifact of our fitting procedure.

4.1.2. Stellar Dispersion Drop

The AGN is the primary source of uncertainty in our modeling of σ_* in the galaxy center. Contamination from the nonthermal central source dilutes the stellar signal, and is degenerate with σ_* (e.g., Greene & Ho 2006). First, we look at the S/N of the dispersion measurements as a function of position. We find that the S/N is always >5 except within 0.″2 of the AGNs. This first test suggests that our measurements at ∼1″ (100 pc) should not be dominated by the AGNs. Next, we re-run pPXF, but instead of fitting the continuum with the default polynomial of the order of 4, we only allow a first or second-order polynomial (Figure 3). While it is clear that, particularly in the case of the first-order polynomial, we achieve very poor fits to the nuclear region ($\lesssim$0.″2), we still find significant evidence for an asymmetric σ-drop. We then return to the Wallace templates (rather than our default SINFONI templates) and try restricting the template set to K dwarfs. We find the same result. Finally, we examine our fits with the template fixed to the mixture derived from the high S/N fit described in Section 4.1. In all of these cases, although the dispersion profile within 0.″5 is not well determined, we recover the σ-drop on 1″ (100 pc) scales. We therefore conclude that the observed drop is real and that the asymmetry results from patchy reddening. Although in general the north side of the disk is more heavily extincted (Section 4.2.3), there are also dust lanes extending to the south, which are apparently preferentially affecting the west side of the 100 parsec-scale disk.

A falling dispersion toward the center of megamaser disk galaxies is not unexpected. These so-called σ-drops are common in both spiral (e.g., Bottema 1993; Emsellem et al. 2001; Falcón-Barroso et al. 2006; Peletier et al. 2007; Riffel et al. 2011), and early-type galaxies (Pinkney et al. 2003; Emsellem et al. 2004; Lyubenova et al. 2008) often associated with nuclear star clusters (Lyubenova et al. 2013). The typical scale is ∼200 pc, and the most likely explanation for the falling dispersion is that the galaxy harbors a gas disk that is currently or was recently forming stars. These bright, dynamically cold stars dominate the central dispersion and cause σ_* to fall. In fact, NGC 2273, one of the nearer megamaser disk galaxies, has a dramatic σ-drop that coincides with a known disk in the inner ∼500 pc (Erwin & Sparke 2003; Barbosa et al. 2006). Hicks et al. (2013) suggest that low central dispersions are more common in active galaxies.

If the σ-drop is caused by a young stellar disk, then we might also expect to see younger stars coinciding with the lower stellar velocity dispersion. We create a median spectrum over the region with $\sigma_* < 80$ km s^{-1}, and rerun pPXF to investigate the mixture of stellar populations using the Wallace templates, which cover a wider range of spectral type. While there is a slight preference for more supergiant light in the region of the σ-drop, we do not find a significant difference in best-fit spectral type as a function of region. The CO EW profile is also quite symmetric and has reached its asymptotic values already in the σ-drop region (Figure 3). With a larger spiral sample, Peletier et al. (2007) also find similar stellar population ages inside and outside of the σ-drop regions.

4.1.3. Stellar Kinematics Summary

We propose that the observed stellar kinematics are the superposition of three distinct components. On kiloparsec-scales, the galaxy disk has P.A. = 90°. Within our 300 pc aperture, the kinematics are dominated by the hotter bulge/bar (Veilleux et al. 1999a). Based on the highest σ_* measurements within the cube, presumably occurring where dust obscuration is highest, we measure $\sigma_* \approx 125$ km s^{-1} in the bulge/bar. Then, within the inner 100 pc, we see evidence in both the kinematics and the NIR isophotes for a nuclear disk component at a P.A. ≈ 75°, misaligned by ∼15° from the large-scale disk and with a $V/\sigma \approx 1$. Finally, on parsec scales, there is a masing disk at P.A. = 110°, which is misaligned not only from the kiloparsec-scale disk, but also by ∼35° from the nuclear stellar disk (Greene et al. 2013).

4.2. Gas Fluxes and Kinematics

With a best-fit stellar rotation field in hand, we turn to the gas kinematics. We will examine three transitions: H_2 2.12 μm 1-0S(1), Brγ, and the coronal line [Si VI] λ1.96 μm. We note that the [Ca VIII] λ2.32 μm line, also coronal, has been used

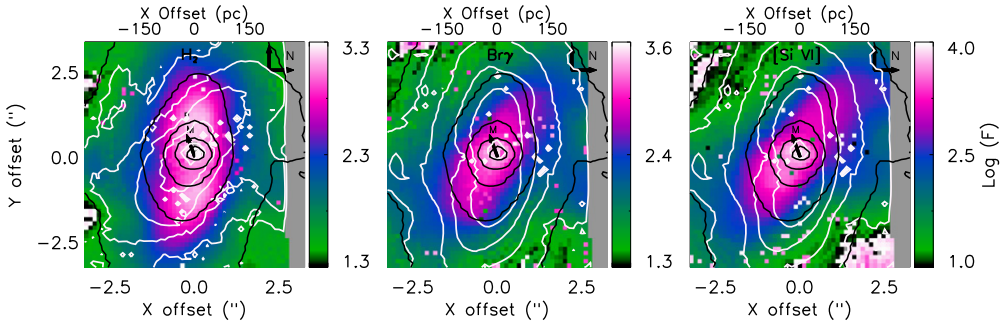

Figure 5. We show the integrated flux in H_2 2.12 μm (left), Brγ (middle), and [Si VI] (right) for the SINFONI data cube. In black contours we show the galaxy continuum (same for all panels). In white, for comparison we show the Brγ flux (left) and the H_2 flux (middle and right). Since the data are not flux calibrated, the flux scale is arbitrary. Note first of all the very different flux distributions for the molecular hydrogen and the other two lines. Specifically, the H_2 is oriented E–W along the nuclear disk seen in the *HST* imaging, while the other lines are at an angle nearly perpendicular to the maser disk, that matches the inner jet. It is also interesting to note that the H_2 distribution is quite asymmetric. Very likely the same extinction that hides the W side of the nuclear stellar disk and causes the asymmetric σ-drop is also causing this asymmetric distribution in the molecular gas. In contrast, the [Si VI] and Br γ are symmetric in the center, and if anything are brighter toward the west.

(A color version of this figure is available in the online journal.)

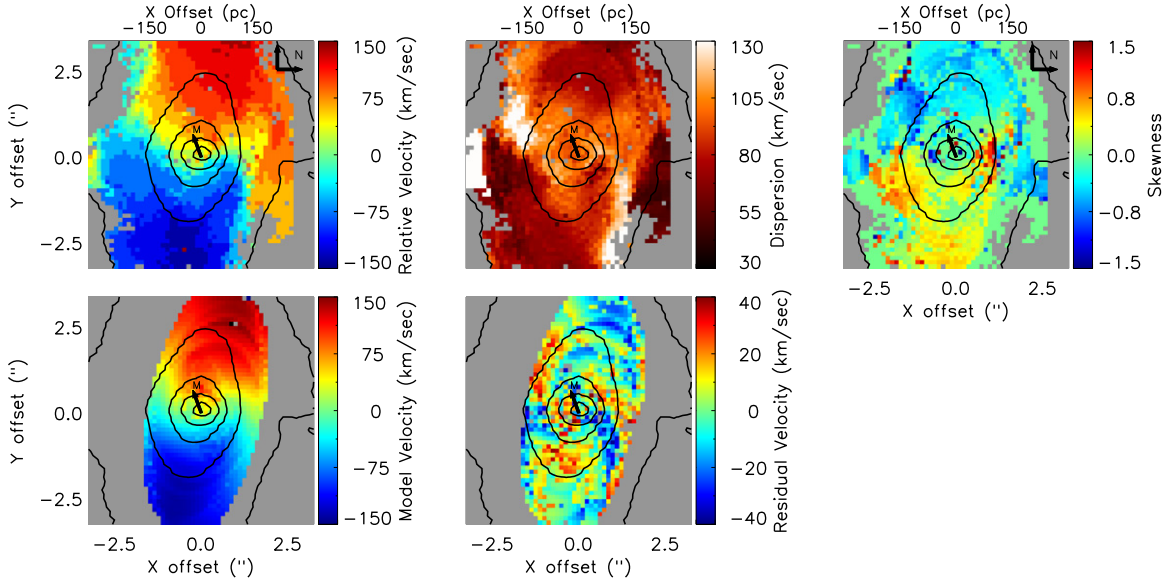

Figure 6. In the top row, we show the H_2 2.12 μm velocity (left), dispersion (middle), and skewness (right) fields. On the bottom row, we show the best-fit circular velocity from a tilted-ring model using *kinemetry* (left), and the difference between the velocity field and the model (right). The contours are continuum flux density, as in Figure 3. The orientation of the cube has north to the right and east up, as shown, and we also indicate the orientation of the megamaser disk on sub-parsec scales (107°). The rotation field shows a kink in the center, with the inner P.A. intriguingly close to that of the maser disk. There are corresponding spiral-shaped arms of high dispersion, and a three-armed pattern in the model residuals. All of these may be signatures of a nuclear disk, inflow/outflow out of the plane of the disk, or possibly the inward extension of the large-scale bar.

(A color version of this figure is available in the online journal.)

to trace the NLR (e.g., Storchi-Bergmann et al. 2009), but is blended with the CO bandhead. Thus we choose to focus on the [Si VI] line here. The two-dimensional velocity and line-ratio fields will provide information about the origins and excitation mechanisms of each transition. The fluxes that we present are the integrated flux from our one or two Gaussian models as described in Section 3.3. We calculate the FWHM non-parametrically from the sum of both components, and the dispersions are simply calculated as FWHM/2.35. We also measure and present the skewness of the lines, which encapsulates the asymmetry in the two-component fits.

In Figure 5, we show the distribution of fluxes in the H_2, Brγ, and [Si VI] emission lines, while in Figures 6–8, we summarize their kinematics. We see that the overall morphology of the H_2 follows the stellar continuum, and is even more flattened than the stellar distribution, suggesting that the emission arises from the nuclear disk. Furthermore, close inspection reveals that the H_2 emission is asymmetric, being considerably brighter towards the East. The brighter side of the H_2 disk is coincident with the observed σ-drop in the stellar distribution; we can directly see the extinction of the H_2 in the region where the σ-drop is also extincted. In contrast, the high-ionization lines are oriented at P.A. $\approx 30°$, aligned with the jet on similar scales, and also with the [O III] emission that traces the narrow-line region (NLR; Figure 7). The Brγ mostly follows the high-ionization lines (Figure 8). Their light distribution strongly suggests that their emission arises in front of the disk in projection, since the [Si VI] is actually brighter towards the West (similar to the [O III]). Based partially on these flux distributions, as well as the kinematics and line ratios presented below, we will suggest that the H_2 mainly traces star formation in the nuclear disk, while Brγ and [Si VI] trace the NLR (e.g., Rodríguez-Ardila et al. 2004; Storchi-Bergmann et al. 2009; Riffel & Storchi-Bergmann 2011; Mazzalay et al. 2013b).

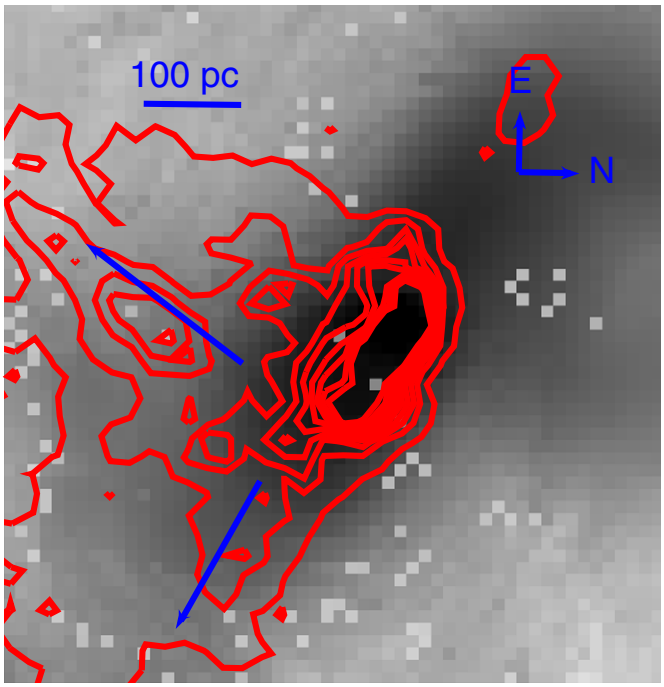

Figure 7. Correspondence between the optical and NIR high-ionization lines. In grayscale, we show the [Si VI] emission map over the same field of view displayed in all other maps above. We use [Si VI] to represent the purest and highest S/N view of the NLR as traced by emission lines within our cube. The narrow-band [O III] λ5007 Å image from *HST* is overlaid as red contours. The scale bar indicates 1″ (∼100 pc). The blue arrows schematically indicate the edges of the ionization cone that we see hints of in the [Si VI] and Brγ maps. The radio emission as imaged by Falcke et al. (1998) follows the ionized gas closely on these scales, and then opens into a plume to the north–east (off of this image).

(A color version of this figure is available in the online journal.)

4.2.1. Molecular Hydrogen Kinematics

We focus first on the H_2 2.12 μm kinematics (Figure 6). As with the stellar kinematics above, we fit the H_2 velocity field using kinemetry. The best-fit rotation curve, P.A., and eccentricity are shown in blue in Figure 4. With $V/\sigma \approx 1.5$ the gas is considerably colder than the stars, but we are not seeing pure rotation. The rotation field shows an *S*-shaped kink. The twist is apparent as a discontinuity in the H_2 ellipticity ϵ and P.A. in the rotation profiles at 1.″5 (150 pc), a similar radius to the changing stellar kinematics. In the skewness map, along the high-dispersion kink, we see a tendency for red asymmetry, which is plausibly attributed to the superposition of two velocity components. Interior to the twist, the kinematic PA of the gas on <150 pc scales appears to align with the megamaser disk. Thus, it is possible that whatever mechanism causes this kink is responsible for fueling material on parsec scales.

On the same scales, we find a two-armed spiral in the dispersion map, with an inner P.A. $\approx 30°$. We find a corresponding three-arm spiral pattern in the residual map by subtracting the best-fit rotation model from the observed velocity field. To interpret these trends, we recall that any $m = 2$ mode perturbation can cause $m' = 2$ deviations in the even velocity moments, including density and dispersion, and due to geometry $m' = 3$ (and $m' = 1$) deviations in the odd velocity moments (e.g., Canzian 1993). We propose a few mechanisms that may explain these kinematic properties.

First, in the study by van de Ven & Fathi (2010) of the inner region of NGC 1097, similar signatures were explained as the result of a two-arm nuclear spiral in the disk plane (see also Davies et al. 2009). Given that the nuclear disk in NGC 4388 is nearly edge-on, such a co-planar spiral density wave seems unlikely. The second possibility is that we are seeing the superposition of the kiloparsec-scale disk and the 100 pc nuclear disk that we saw in the stellar kinematics. However, the gas P.A. $\approx 110°$, while approximately aligned with the maser disk on sub-parsec scales, does not align with the stellar disk of P.A. $\approx 75°$. The final possibility is that the twist we observe here is related to the kink from the bar observed on kiloparsec scales (e.g., Veilleux et al. 1999a). Only with our upcoming AO observations can we address the <100 pc gas kinematics definitively, and hopefully help determine what is driving the gas inward toward the AGNs.

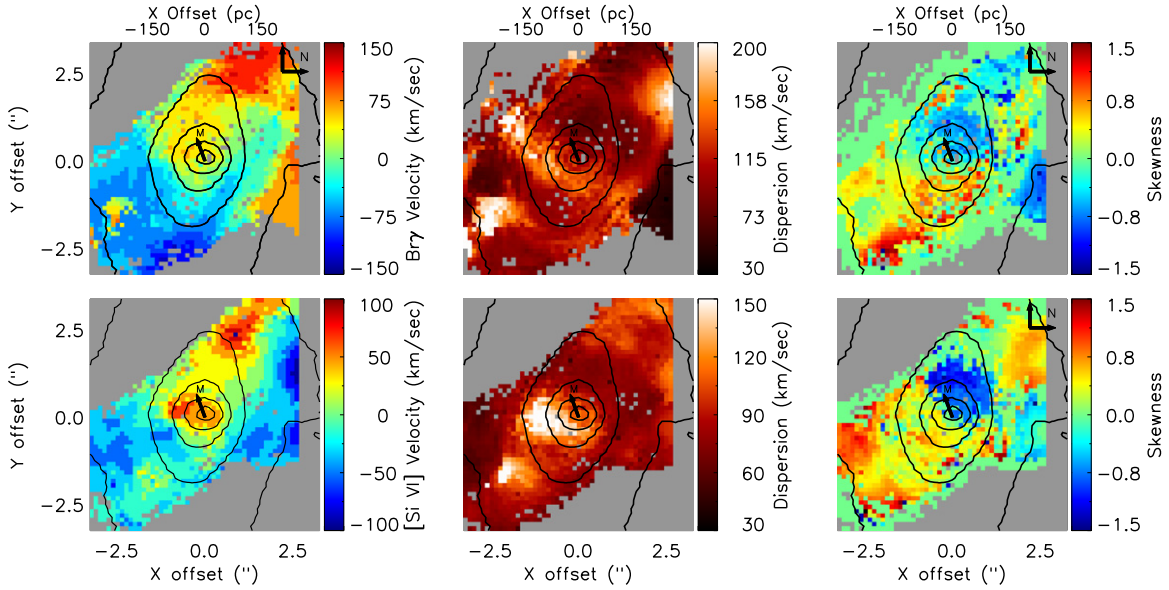

Figure 8. Two-dimensional gas velocity (left) and dispersion (right) for Brγ (top) and [Si VI] (bottom), contours show galaxy continuum as above. In all cases, the images are aligned with west up and north to the left, to match the data cube itself. The molecular hydrogen (Figure 6) is aligned with the kiloparsec-scale disk of the galaxy, while these transitions are more closely aligned with the parsec-scale radio jet.

(A color version of this figure is available in the online journal.)

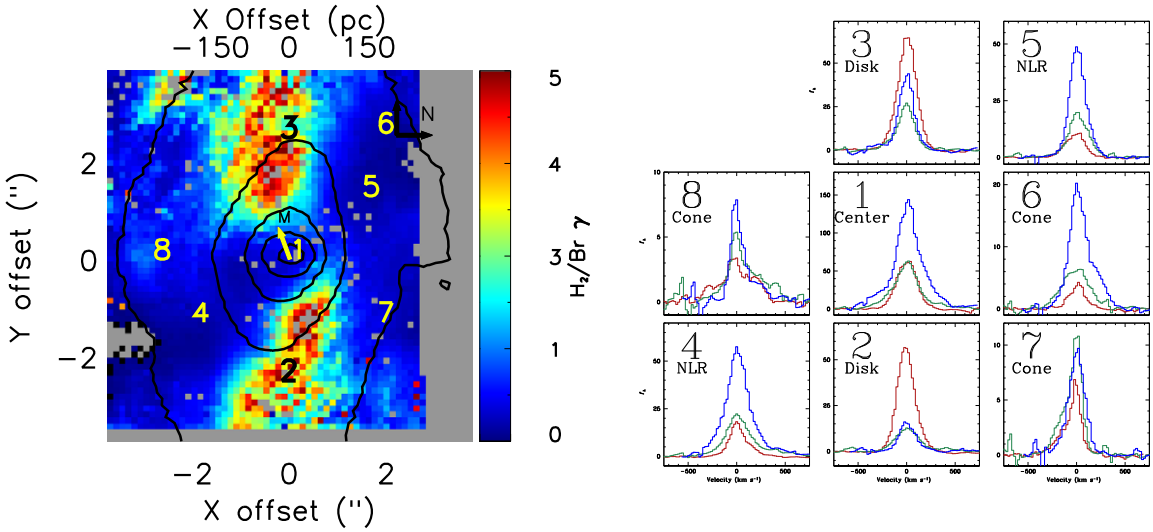

Figure 9. Left: the H_2 $\lambda 2.12\,\mu$m/Brγ ratio. The values are high in the disk, and quite low along the jet/NLR direction, perpendicular to the maser disk. Each number marks a region that we have extracted to create higher S/N spectra. Right: spectra in each region, of H_2 1–0S(1) (2.12 μm; red), Brγ (green), and [Si VI] (blue). The flux normalizations are arbitrary, but the spectra span 700 km s^{-1} in velocity on either side of systemic.

(A color version of this figure is available in the online journal.)

4.2.2. Molecular Hydrogen Excitation

The H_2 shows very regular rotation along the orientation of the large-scale galaxy disk outside of the inner 1″ (100 pc). Additional information is encoded in the ratios of H_2 to Brγ (Figure 9), and ratios of different H_2 transitions (Figure 10). Typically, in the hard ionizing field of the NLR, the ratio of H_2 to Brγ takes a value $0.6 < H_2/\mathrm{Br}\gamma < 2$, while it is $\leqslant 0.6$ in star-forming regions (Larkin et al. 1998; Moorwood & Oliva 1990; Rodríguez-Ardila et al. 2004, 2005; Riffel et al. 2010). Finally, in dense spiral arms, even higher ratios of $H_2/\mathrm{Br}\gamma > 2$ are observed. Riffel et al. (2013a) suggest that the increased H_2 emission arises from the higher gas densities within spiral arms (see also Riffel et al. 2013b). NGC 4388 obeys these trends in general (Figure 9). Along the disk, the H_2 is strong, and the ratio has values >2, as is commonly seen in spiral arms, while in the galaxy center, the line ratio ranges from $0.6 < H_2/\mathrm{Br}\gamma < 1$, values common for Seyfert galaxies.

The only surprising region lies off the disk along a ∼60° angle east of north above and below the galaxy plane, where the Brγ emission is strongest. Here, the $H_2/\mathrm{Br}\gamma$ ratio is very low >0.5. Such low ratios are reportedly associated with star-forming regions (e.g., Moorwood & Oliva 1994; Larkin et al. 1998; Rodríguez-Ardila et al. 2004, 2005; Riffel et al. 2013a). However, in this case, the Brγ and [Si VI] morphologies match both the orientation of the radio jet and the NLR traced by [O III] λ5007 in the optical. Thus, we suggest that the low H_2 relative to Brγ in these regions is instead due to very low densities of the NLR (Dors et al. 2012).

We now construct spectra in characteristic regions to examine both the H_2 line ratios and the line kinematics. We select regions of the map based on the $H_2/\mathrm{Br}\gamma$ line ratio and construct high S/N spectra from the continuum-subtracted cubes. Region 1 is the center, defined as all pixels with CO EW $\leqslant$ 6 Å that lie within 1.″5 of the center. We extract two regions in the disk ($H_2/\mathrm{Br}\gamma < 0.6$; regions 2 and 3) and two regions in the NLR ($H_2/\mathrm{Br}\gamma > 1$; regions 4 and 5). Finally, we sample gas that falls beyond the main galaxy and overlaps with the [O III] ionization cone (region 8), as well as two regions North of the disk, toward the Northern radio lobe (regions 6 and 7). The extracted spectra for the strong transitions (H_2 2.12 μm, Brγ, and [Si VI]) from each region are shown in Figure 9, the spectra from different H_2 transitions are shown in Figure 10, and measured properties from these spectra are presented in Table 1. Because we fit the lines using an instrumental profile, the linewidths are naturally corrected for instrumental resolution. Each line is fitted independently. In fact, as shown in Figure 10, the centroids and line shapes for the different transitions can differ, particularly for regions in the NLR ionization cone.

For each region, we can ask about the excitation mechanisms of the H_2. There are two ways to excite the warm H_2: thermal processes or fluorescence via UV heating. The thermal processes that can in principle heat the gas include shocks, X-ray emission, or heating by UV emission.

The predicted line ratios of various H_2 transitions provide diagnostics of the primary excitation mechanism. Specifically, if fluorescence dominates the excitation, then the ratio of H_2 2–1S(1) 2.25 μm/1–0S(1) 2.12 μm is expected to be ∼0.5–0.6 while the 1–0S(2) 2.03 μm/1–0S(0) 2.22 μm ratio is expected to be ∼1 (Black & van Dishoeck 1987). We show this pair of ratios and the expectation for pure thermal emission as the solid line, while the region dominated by fluorescence is shown schematically with the large X at the lower right in Figure 10. There is room for some UV fluorescence, but these line ratios suggest that the bulk of the excitation is thermal. Similar conclusions have been drawn for larger samples of Seyfert galaxies (Veilleux et al. 1997; Quillen et al. 1999; Rigopoulou et al. 2002).

Our excitation diagram is constructed for the integrated line profile but, in fact the line ratio is clearly a function of velocity, particularly for the line emission arising from the NLR ionization cones. We do not have sufficient S/N to construct line ratios for the line core and line wings separately, but these different line shapes are pointing to different dominant excitation mechanisms in the line wings. Higher S/N is needed to quantitatively examine velocity-dependent line ratios.

We are still left with the question of which thermal process dominates the excitation. Previous work has drawn various conclusions, with Veilleux et al. (1997) for instance favoring shocks in outflows, Quillen et al. (1999) favoring a mix of

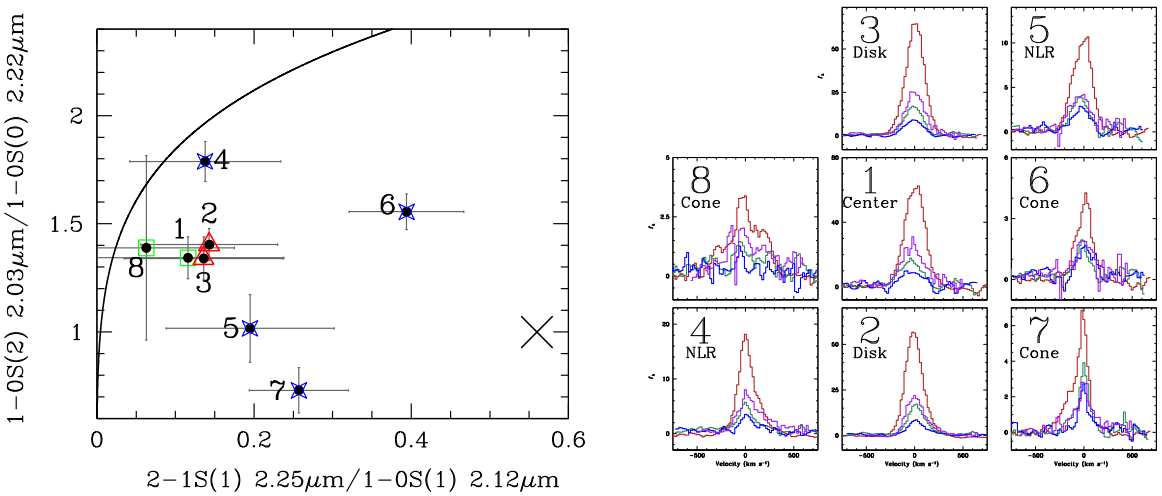

Figure 10. Left: H_2 line ratio diagram, comparing the ratio of H_2 2–1S(1) 2.25 μm /1–0S(1) 2.12 μm to the ratio of H_2 2-0S(2) 2.03 μm/1-0S(0) 2.22 μm. The solid line shows the theoretical expectation for pure thermal excitation, while the large black cross schematically shows the region occupied by pure fluorescence models in Black & van Dishoeck (1987). The measurements are made on the spectral regions described in the text (Section 4.2.2) and in Table 1, and have been divided into those with low ratios of H_2/Brγ ($\leqslant$0.6; blue stars), medium ratios between 0.6 and 2 (green squares), and high ratios greater than 2 (red triangle). The first is characteristic of star forming regions, the second of Seyfert galaxies, and the final of LINERs. Right: we show the spectra of all four H_2 transitions in each region. The strongest (red) is H_2 1–0S(1) 2.12 μm, next (purple) is H_2 2–0S(2) 2.03 μm, then (green) H_2 1–0S(0) 2.22 μm, and finally the weakest (blue) is H_2 2–1S(1) 2.25 μm. The velocity structure of all transitions is very similar in the disk, while there are interesting differences in the NLR and ionization cone regions. Particularly note that in region 7, the 1–0S(1) line has a blue wing while the 2–1S(1) line has a red wing.

(A color version of this figure is available in the online journal.)

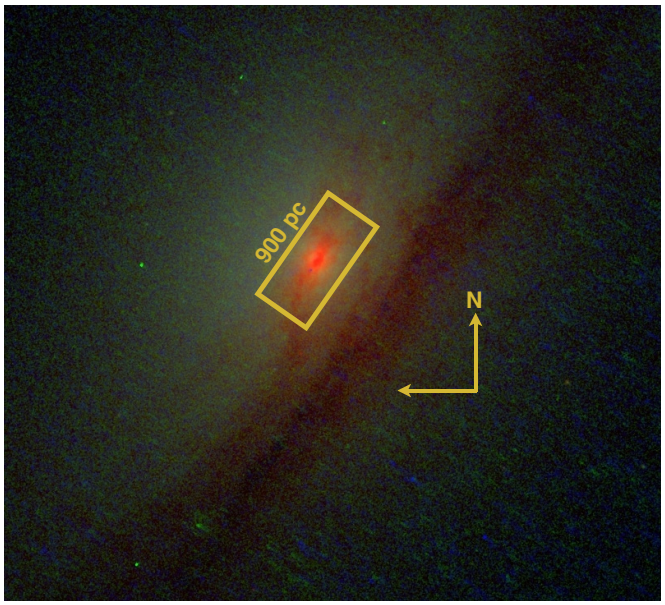

Figure 11. Three-band *HST*/WFC3 image of NGC 1194 including F336W, F438W, and F814W (Greene et al. 2013). As indicated, north is up and east to the left in this image. We show the OSIRIS field of view (3.2 × 1.″2 or 900×340 pc) with the yellow box, oriented along the major axis of the galaxy as our observation was.

(A color version of this figure is available in the online journal.)

processes including emission from photo-dissociation regions, Storchi-Bergmann et al. (2009) favoring X-ray heating or shocks, and so on. Recent papers have favored X-ray heating in the vicinity of an AGN (e.g., Hicks et al. 2009). However, in our case, the fact that there is little H_2 coming the NLR while the bulk of the H_2 emission on these scales follows the morphology of the starlight (Figure 5) strongly suggests that the H_2 is predominantly excited by stellar processes (e.g., UV radiation and/or shocks from supernovas) rather than the AGNs.

4.2.3. The Narrow-line Region

Bridging the gap between the accretion flow on <parsec scales and the large-scale ionized gas outflow, we can examine the ionized gas emission on 100 pc scales. In this region, the radio emission is complex, extends predominantly north–south (perpendicular to the disk) and contains two unresolved peaks and a more diffuse "bubble" to the north (Stone et al. 1988; Hummel & Saikia 1991). Falcke et al. (1998) show that the Northern radio source is coincident with the optical nucleus, while the southern radio knot is coincident with a bright region of ionized gas seen in [O III], strongly suggesting a jet–ISM interaction. High-ionization gas is present to the south of the nucleus in our data cubes as well. Previous near-infrared spectra (e.g., Winge et al. 2000; Knop et al. 2001; Imanishi 2003) show extended H_2 coincident with the galaxy disk, and high-ionization gas emission from Brγ and [Si VI] coincident with the nucleus and ionization cone. With our high spatial resolution and three-dimensional coverage, we can robustly disentangle the disk and NLR kinematics.

The Brγ and [Si VI] emission lines show similar spatial distributions that parallel the NLR emission seen in [O III] (Figures 5 and 7). Their emission is distributed at an angle of P.A. $\approx$ 30°, tracing the general orientation of the radio jet seen on similar scales (Falcke et al. 1998). The ionization cone seen in [O III] continues to the south–west beyond the SINFONI field of view (Pogge 1988; Veilleux et al. 1999a; Stoklasová et al. 2009), and is filled with radio plasma (Falcke et al. 1998). To the north, beyond our field of view, the jet opens into another wide angle fan. It is likely that the southern ionization cone sits in front of the galaxy disk, while the northern one (which we can see in this map and in the radio but not in the optical) is extincted by the galaxy disk.

In Figure 8, we show the velocity and FWHM fields for Brγ and [Si VI]. Both the morphology and the kinematics differ from that seen in the H_2. Specifically, we do not see coherent rotation in either transition. The skewness plots are also interesting.

Table 1
Line Fits by Region

Region (1)	Type (2)	FWHM$_{H_2}$ (3)	FWHM$_{Br\gamma}$ (4)	FWHM$_{(Si\ VI)}$ (5)	$H_2/Br\gamma$ (6)	2.25/2.12 (7)	2.03/2.22 (8)
1	center	249 ± 12	274 ± 14	275 ± 22	0.85 ± 0.11	0.11 ± 0.12	1.34 ± 0.09
2	disk	213 ± 10	273 ± 13	191 ± 9	3.16 ± 0.10	0.14 ± 0.08	1.40 ± 0.07
3	disk	222 ± 11	192 ± 9	183 ± 9	2.63 ± 0.18	0.13 ± 0.10	1.34 ± 0.09
4	NLR	183 ± 9	270 ± 13	249 ± 18	0.47 ± 0.09	0.13 ± 0.09	1.78 ± 0.09
5	NLR	241 ± 12	222 ± 14	190 ± 9	0.51 ± 0.11	0.19 ± 0.10	1.01 ± 0.15
6	cone	159 ± 7	336 ± 16	216 ± 10	0.31 ± 0.09	0.39 ± 0.07	1.55 ± 0.08
7	cone	126 ± 6	144 ± 11	195 ± 9	0.55 ± 0.04	0.25 ± 0.06	0.73 ± 0.10
8	cone	434 ± 88	166 ± 13	144 ± 7	0.75 ± 0.05	0.06 ± 0.11	1.38 ± 0.42

Notes. Column 1: region (as shown in Figure 9). Column 2: type of region, where disk and NLR are self-explanatory, and cone means in the ionization cone extending to the south–west. Column 3: FWHM of H_2 $\lambda 2.12\,\mu$m (km s^{-1}). Column 4: FWHM of Brγ (km s^{-1}). Column 5: FWHM of [Si VI] (km s^{-1}). Column 6: H_2 1–0$S(1)$ 2.12 μm/Brγ. Column 7: $H_2$2–1$S(1)$ 2.25 μm/H_2 1–0$S(1)$ 2.12 μm. Column 8: $H_2$1–0$S(2)$ 2.03 μm/H_2 1–0$S(0)$ 2.22 μm.

In both transitions, we see redshifted gas toward the south–west and blue-shifted gas toward the north–east. Our interpretation is that we are seeing bulk motion of the gas along the jet, which apparently points toward us to the north and away from us to the south of the galaxy disk. In both cases, we are probing the region of the NLR where the jet has "broken-out" of the galaxy disk. The higher velocity gas is moving along the walls of the bicone, as accelerated by the jet (e.g., Storchi-Bergmann et al. 2010; Riffel et al. 2013b).

The coadded spectra from different regions reveal a similar story. In the disk regions (regions 2 and 3), where there is little emission from the NLR gas, we find strong and narrow H_2, and weak, but rather broad, Brγ and [Si VI]. In the NLR regions (4 and 5), Brγ and [Si VI] are stronger and slightly broader than in the disk regions. The line profiles are most complex at positions 6, 7, and 8, regions that are also bright in [O III] emission and where we see the strongest skewness in the lines (Figures 7 and 8). We clearly see the red wing in the spectra from regions 6 and 8, and the corresponding blue wing in the spectra from region 7.

Again in line with recent work (e.g., Storchi-Bergmann et al. 2010), we find that the high-ionization lines and hydrogen recombination lines trace "feedback." That is, the emission in these lines is dominated by extraplanar gas likely excited by the AGNs, and perhaps entrained by the nuclear jet. This NLR emission is also aligned roughly perpendicular to the megamaser disk on sub-parsec scales.

Finally, we ask whether there is a broad component to the Brγ, since Ho et al. (1997) detect a weak broad base to the Hα line in NGC 4388, with a FWHM of 3900 km s^{-1}. Within the central nuclear point source emission, all the species have lines that are broad and symmetric (Table 1). However, we find no evidence for a true broad-line component in Brγ. Instead, all the transitions have comparable widths. Neither Veilleux et al. (1997) nor Lutz et al. (2002) detect broad emission from Brγ or Brα in their long-slit NIR spectra either. Perhaps the broad component detected in the optical is scattered broad emission rather than directly transmitted light (e.g., Liu et al. 2009).

5. NGC 1194

NGC 1194 is an inclined ($i \approx 90^\circ$) S0 galaxy at $D = 57.9$ Mpc. The galaxy P.A. is 145°, and we aligned the IFU along the major axis. Given our PSF of ∼0.″16, we are resolving 40 pc scales with our AO-assisted observations. Thus we achieve very comparable spatial resolution to the NGC 4388 observations presented above. We have detected the large-scale disk in NGC 1194 in H I, and find a circular velocity of 220 ± 20 km s^{-1} (Sun et al. 2013). From SDSS imaging, we find a bulge-to-total ratio of 0.5 ± 0.2 (Greene et al. 2010).

The BH in NGC 1194 has a mass of $6.5 \pm 0.4 \times 10^7\ M_\odot$, one of the most massive in the megamaser disk sample. NGC 1194 is in the *IRAS*-selected 12 μm sample (Rush et al. 1993), and in the *Swift*/BAT 22 month sample (Tueller et al. 2010). It has a hard X-ray luminosity of $\log L_x = 43.2$ from 14–195 keV, but is not Compton thick (Georgantopoulos et al. 2011). Depending on the bolometric correction, the Eddington ratio is $\approx 10^{-3}$ to 10^{-2} (Vasudevan et al. 2009), considerably lower than NGC 4388. The galaxy was also part of the *HST*/[O III] snapshot survey of Schmitt et al. (2003). They find extended [O III] emission with an extent of 700 pc along the major axis of the galaxy, and 470 pc along the minor axis. The nucleus was detected in FIRST and at 8.4 GHz by Thean et al. (2000), with a flux density of 0.9 mJy, and an upper limit on the radio core size of 52 pc.

There are three existing *K*-band spectra of NGC 1194 (Sosa-Brito et al. 2001; Imanishi & Alonso-Herrero 2004; Davies et al. 2005) on ∼1″ (900 pc) scales. In all cases the CO bandhead is detected, but the line emission is very weak. Davies et al. do not detect Brγ, but marginally detect the H_2 $\lambda 2.12\,\mu$m line.

5.1. Stellar and Gas Kinematics

Due to the heavy binning required to achieve adequate S/N, we cannot derive much spatially resolved information for this galaxy. In terms of the gas, the Brγ and [Si VI] flux distributions are very centrally concentrated, with a FWHM that is consistent with that of the continuum. The H_2 $\lambda 2.12\,\mu$m emission is clearly extended, but the distribution is quite patchy. We therefore construct average spectra in annuli, taking the central spectrum within the FWHM of the PSF (0.″16). Then we construct six spectra with outer radii of 0.″5, 1″, and 1.″5 (140, 280, and 420 pc), respectively, on either side of the galaxy minor axis. Three examples of these spectra are shown in Figure 12.

We can measure the radial velocities and stellar velocity dispersions reliably in these coadded spectra, using pPXF as above. We do find that the stars are rotating, with an amplitude of ∼100 km s^{-1} (Figure 13). In contrast, we do not detect a clear rotation curve in the gas. Instead, the velocities are very asymmetric. Asymmetric velocities in high-ionization lines are often attributed to outflow (e.g., Müller-Sánchez et al. 2011; Mazzalay et al. 2013a), and are sometimes seen in H_2 as well (e.g., Riffel & Storchi-Bergmann 2011), which may be

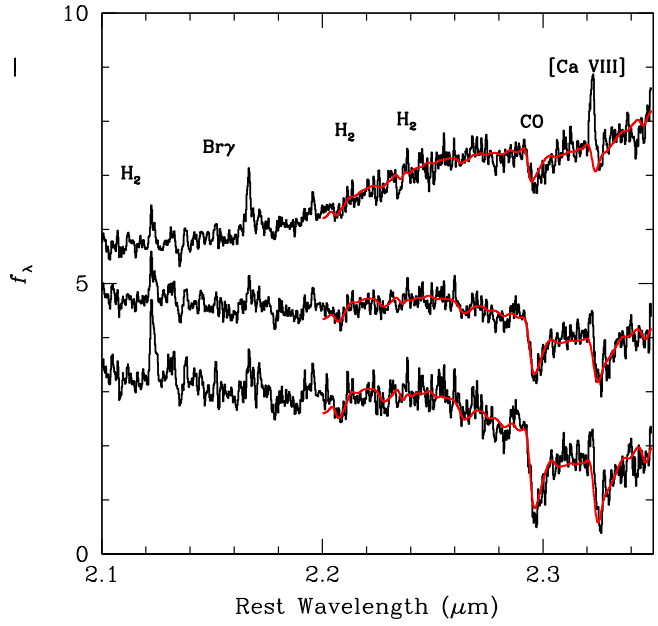

Figure 12. Three spectra from the NGC 1194 data cube; due to telluric residuals, we do not show the region from 1.95 to 2.1 μm. From top to bottom, we show spectra within the inner 0.″18 (50 pc), between 0.″2 and 0.″5 (140 pc), and then 0.″5 to 1″ (140–280 pc). Going from the center outward, we can see the continuum change from AGN-dominated to galaxy-dominated, the H_2 equivalent width increases, and the [Ca VIII] line strength decreases. These trends are qualitatively similar to NGC 4388 above, although we have far less detailed spatial information. In red, we overplot our best-fit composite stellar template over the restricted region that we fit, and as above the strong emission lines were masked in the fit.

(A color version of this figure is available in the online journal.)

the explanation here. Another possibility is that we are seeing spiral arms or some other nonaxisymmetric gas distribution that is unrelated to the AGN. Our limited S/N prevents us from distinguishing between these cases. Neither the [Si VI] nor the Brγ is spatially extended enough to measure reliable velocities beyond the central region.

5.2. Gas Emission Lines

All of the gas emission line fluxes are weak, and the intrinsic luminosities are also low. It is perhaps not surprising that this S0 galaxy is gas poor compared to NGC 4388 above, based simply on their respective morphology. On the other hand, the center of NGC 1194 is quite dusty, so there must be some associated gas, and indeed we detect atomic hydrogen in this galaxy on large scales (Sun et al. 2013). The strongest gas emission comes from the high-ionization [Si VI] line, but as mentioned above it is only marginally spatially resolved. Thus, we suspect that the emission from this transition and Brγ emerge from the inner NLR. In contrast, the H_2 is clearly spatially resolved. In analogy with NGC 4388 above, these different gas morphologies may be suggesting that the H_2 is excited by both the AGNs and stellar processes. We also measure the spatially resolved ratio of H_2/Brγ, and find that the ratio is lowest in the galaxy center (having AGN-like values) and then rises outward, perhaps indicating an increased contribution to the H_2 from stellar processes. These line ratios may suggest that the asymmetric velocities we observe in the H_2 are due to non-circular motions in the inner regions of the galaxy (e.g., spiral arms) rather than outflow.

6. SUMMARY

We have analyzed integral-field *K*-band observations of two megamaser disk galaxies. Our data probe ∼50 pc scales in both galaxies, and thus allow us to study the distributions of stars and gas at the centers of these galaxies to investigate AGN fueling. In NGC 1194, an S0, there is very little gas, and with our S/N ratios, we cannot say much about the two-dimensional velocity or dispersion fields. However, in NGC 4388, we have excellent S/N, and uncover a variety of interesting features.

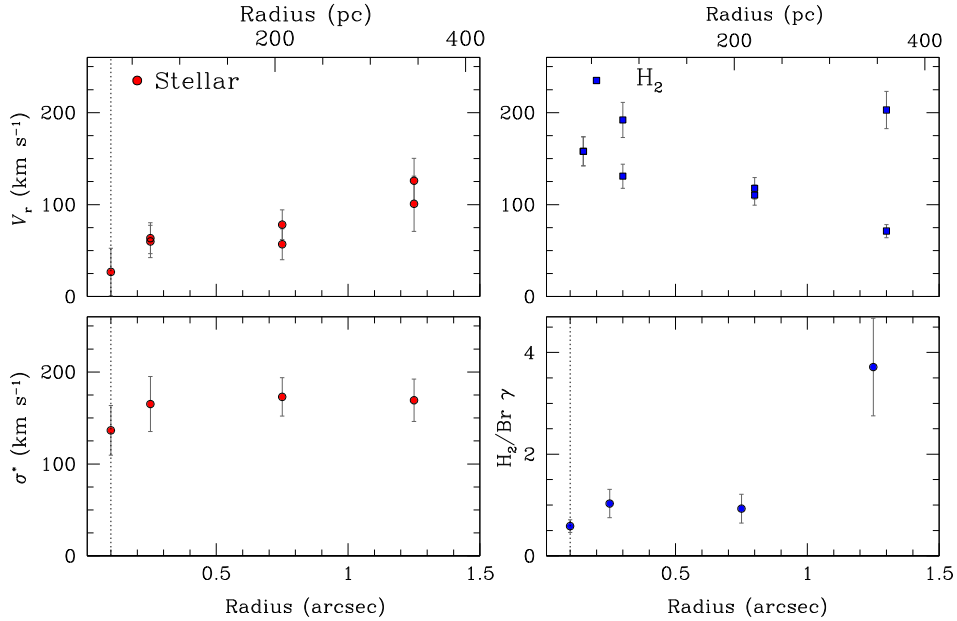

Figure 13. NGC 1194 data have considerably lower S/N than the NGC 4388 data. We have binned the spectra into seven zones, including the nucleus within the central 0.″16, and then three annuli of width 0.″5 on either side of the galaxy, extending along the major axis of the galaxy. The velocity and dispersion are measured individually for each of these bins. We examine the stellar and H_2 rotation curves (top). We also show the stellar velocity dispersion (bottom left) as a function of radius, measured from radial bins (e.g., folding about the major axis). Finally, we show that the ratio of H_2 to Brγ rises dramatically from the center where it is AGN-dominated to the disk at larger radius (bottom right).

(A color version of this figure is available in the online journal.)

1. The stellar velocity field demonstrates well-ordered rotation aligned with the kiloparsec-scale disk. Although there is net rotation in the stars, still they are kinematically hot, with $V/\sigma \approx 0.6$, likely dominated by the dispersion in the kiloparsec-scale bulge.
2. In the inner $1''$ (100 pc), we also see evidence for a nuclear disk, offet in P.A. by 15° from the kiloparsec-scale disk. The evidence includes disky isophotes in the *HST*/WFC3 F160W image and a distinct drop in stellar velocity dispersion on one side of the putative disk (the other side apparently extincted). Features like this, so called σ-drops, have been seen in the centers of a number of nearby spirals (e.g., Emsellem et al. 2001; Peletier et al. 2007), and there is some hint that they are more common among actively accreting galaxies (Hicks et al. 2013). We note that this 100 parsec-scale nuclear disk is misaligned by $\sim 35^\circ$ from the megamaser disk on sub-parsec scales.
3. The H_2 gas also shows regular kinematics on >100 pc scales, with a well-defined rotation field that is aligned with the kiloparsec-scale disk. With a higher rotation amplitude, the gas is considerably colder than the stars ($V/\sigma \approx 1.5$). We also see a kink in the rotation curve on ~ 100 pc scales. Intriguingly, the H_2 rotation within 100 pc appears to align with the megamaser disk. However, the physical origin of the kinematic twist is not yet clear.
4. Based on H_2 diagnostic line ratios, we conclude that the molecular hydrogen is mainly excited by thermal processes. Based on the morphology and kinematics of the H_2 gas, we speculate that these thermal processes are mostly associated with stars rather than radiation from the AGNs (e.g., Storchi-Bergmann et al. 2010; Riffel & Storchi-Bergmann 2011).
5. In contrast, the Brγ and high-ionization lines (particularly [Si VI]) have a completely different spatial distribution and kinematics. They trace the inner narrow-line region, also seen on 500 pc scales in [O III], as well as the 100 parsec-scale jet.

In the future, we hope to analyze a larger sample of megamaser disk galaxies in this manner. Combined with direct tracers of the cold molecular gas (e.g., with ALMA), as well as high-resolution imaging from *HST*, we hope to build a multi-phase map of AGN fueling from 100 to 0.1 pc (Greene et al. 2013).

The referee provided a very thorough review that improved the quality of this manuscript. We thank K. Gebhardt and R. van den Bosch for assistance with the early stages of this project. J.L.W. has been supported by an NSF Astronomy and Astrophysics Postdoctoral Fellowship under award No. 1102845. Some of the data presented herein were obtained at the W. M. Keck Observatory, which is operated as a scientific partnership among the California Institute of Technology, the University of California and the National Aeronautics and Space Administration. The Observatory was made possible by the generous financial support of the W. M. Keck Foundation. The authors wish to recognize and acknowledge the very significant cultural role and reverence that the summit of Mauna Kea has always had within the indigenous Hawaiian community. We are most fortunate to have the opportunity to conduct observations from this mountain. Keck telescope time was granted by NOAO, through the Telescope System Instrumentation Program (TSIP). TSIP is funded by NSF.

REFERENCES

Ann, H. B., & Thakur, P. 2005, ApJ, 620, 197
Balick, B., & Heckman, T. M. 1982, ARA&A, 20, 431
Barbosa, F. K. B., Storchi-Bergmann, T., Cid Fernandes, R., Winge, C., & Schmitt, H. 2006, MNRAS, 371, 170
Bender, R., Saglia, R. P., & Gerhard, O. E. 1994, MNRAS, 269, 785
Binney, J. 1978, MNRAS, 183, 501
Black, J. H., & van Dishoeck, E. F. 1987, ApJ, 322, 412
Bonnet, H., Abuter, R., Baker, A., et al. 2004, in The ESO Messenger, Vol. 117, ed. J. R. Walsh (München: G. Peschke Printing House), 17
Bottema, R. 1993, A&A, 275, 16
Braatz, J. A., Henkel, C., Greenhill, L. J., Moran, J. M., & Wilson, A. S. 2004, ApJL, 617, L29
Braatz, J. A., Wilson, A. S., & Henkel, C. 1997, ApJS, 110, 321
Canzian, B. 1993, ApJ, 414, 487
Cappellari, M., & Copin, Y. 2003, MNRAS, 342, 345
Cappellari, M., & Emsellem, E. 2004, PASP, 116, 138
Cappellari, M., Neumayer, N., Reunanen, J., et al. 2009, MNRAS, 394, 660
Cardelli, J. A., Clayton, G. C., & Mathis, J. S. 1989, ApJ, 345, 245
Cid Fernandes, R., Pérez, E., García Benito, R., et al. 2013, A&A, 557, A86
Combes, F., García-Burillo, S., Casasola, V., et al. 2014, A&A, 565, A97
Corbin, M. R., Baldwin, J. A., & Wilson, A. S. 1988, ApJ, 334, 584
Dahari, O. 1985, ApJS, 57, 643
Davies, R. I. 2007, MNRAS, 375, 1099
Davies, R. I., Maciejewski, W., Hicks, E. K. S., et al. 2009, ApJ, 702, 114
Davies, R. I., Müller Sánchez, F., Genzel, R., et al. 2007, ApJ, 671, 1388
Davies, R. I., Sternberg, A., Lehnert, M. D., & Tacconi-Garman, L. E. 2005, ApJ, 633, 105
Davies, R. I., Tacconi, L. J., & Genzel, R. 2004, ApJ, 602, 148
Dors, O. L., Jr., Riffel, R. A., Cardaci, M. V., et al. 2012, MNRAS, 422, 252
Dumas, G., Mundell, C. G., Emsellem, E., & Nagar, N. M. 2007, MNRAS, 379, 1249
Eisenhauer, F., Abuter, R., Bickert, K., et al. 2003, Proc. SPIE, 4841, 1548
Ellison, S. L., Patton, D. R., Mendel, J. T., & Scudder, J. M. 2011, MNRAS, 418, 2043
Elvis, M., Risaliti, G., Nicastro, F., et al. 2004, ApJL, 615, L25
Emsellem, E., Greusard, D., Combes, F., et al. 2001, A&A, 368, 52
Emsellem, E., Cappellari, M., Peletier, R. F., et al. 2004, MNRAS, 352, 721
Englmaier, P., & Shlosman, I. 2000, ApJ, 528, 677
Erwin, P., & Sparke, L. S. 2003, ApJS, 146, 299
Falcke, H., Wilson, A. S., & Simpson, C. 1998, ApJ, 502, 199
Falcón-Barroso, J., Bacon, R., Bureau, M., et al. 2006, MNRAS, 369, 529
Fedorova, E. V., Beckmann, V., Neronov, A., & Soldi, S. 2011, MNRAS, 417, 1140
Filippenko, A. V., & Sargent, W. L. W. 1985, ApJS, 57, 503
Ford, W. K., Jr., Rubin, V. C., & Roberts, M. S. 1971, AJ, 76, 22
Forster, K., Leighly, K. M., & Kay, L. E. 1999, ApJ, 523, 521
Förster Schreiber, N. M. 2000, AJ, 120, 2089
García-Burillo, S., & Combes, F. 2012, JPhCS, 372, 012050
García-Burillo, S., Fernández-García, S., Combes, F., et al. 2009, A&A, 496, 85
Georgantopoulos, I., Rovilos, E., Akylas, A., et al. 2011, A&A, 534, A23
Greene, J. E., & Ho, L. C. 2006, ApJ, 641, 117
Greene, J. E., Peng, C. Y., Kim, M., et al. 2010, ApJ, 721, 26
Greene, J. E., Seth, A., den Brok, M., et al. 2013, ApJ, 771, 121
Greenhill, L. J., Kondratko, P. T., Moran, J. M., & Tilak, A. 2009, ApJ, 707, 787
Greenhill, L. J., Tilak, A., & Madejski, G. 2008, ApJL, 686, L13
Haan, S., Schinnerer, E., Emsellem, E., et al. 2009, ApJ, 692, 1623
Hanson, C. G., Skinner, G. K., Eyles, C. J., & Willmore, A. P. 1990, MNRAS, 242, 262
Herrnstein, J. R., Moran, J. M., Greenhill, L. J., & Trotter, A. S. 2005, ApJ, 629, 719
Hicks, E. K. S., Davies, R. I., Maciejewski, W., et al. 2013, ApJ, 768, 107
Hicks, E. K. S., Davies, R. I., Malkan, M. A., et al. 2009, ApJ, 696, 448
Ho, L. C., Filippenko, A. V., Sargent, W. L. W., & Peng, C. Y. 1997, ApJS, 112, 391
Ho, L. C., Greene, J. E., Filippenko, A. V., & Sargent, W. L. W. 2009, ApJS, 183, 1
Hoffman, L., Cox, T. J., Dutta, S., & Hernquist, L. 2009, ApJ, 705, 920
Hummel, E., & Saikia, D. J. 1991, A&A, 249, 43
Hunt, L. K., Combes, F., García-Burillo, S., et al. 2008, A&A, 482, 133
Imanishi, M. 2003, ApJ, 599, 918
Imanishi, M., & Alonso-Herrero, A. 2004, ApJ, 614, 122
Iwasawa, K., Fabian, A. C., Ueno, S., et al. 1997, MNRAS, 285, 683
Iwasawa, K., Wilson, A. S., Fabian, A. C., & Young, A. J. 2003, MNRAS, 345, 369

Kim, W.-T., Seo, W.-Y., Stone, J. M., Yoon, D., & Teuben, P. J. 2012, ApJ, 747, 60
Knop, R. A., Armus, L., Matthews, K., Murphy, T. W., & Soifer, B. T. 2001, AJ, 122, 764
Kondratko, P. T., Greenhill, L. J., & Moran, J. M. 2005, ApJ, 618, 618
Krajnović, D., Cappellari, M., de Zeeuw, P. T., & Copin, Y. 2006, MNRAS, 366, 787
Krajnović, D., Bacon, R., Cappellari, M., et al. 2008, MNRAS, 390, 93
Kuo, C.-Y., Braatz, J. A., Reid, M. J., et al. 2013, ApJ, 767, 155
Kuo, C.-Y., Lim, J., Tang, Y.-W., & Ho, P. T. P. 2008, ApJ, 679, 1047
Kuo, C.-Y., Braatz, J. A., Condon, J. J., et al. 2011, ApJ, 727, 20
Larkin, J. E., et al. 2006, Proc. SPIE, 6269
Larkin, J. E., Armus, L., Knop, R. A., Soifer, B. T., & Matthews, K. 1998, ApJS, 114, 59
Liu, X., Zakamska, N. L., Greene, J. E., et al. 2009, ApJ, 702, 1098
Lo, K. Y. 2005, ARA&A, 43, 625
Lodato, G., & Bertin, G. 2003, A&A, 398, 517
Lutz, D., Maiolino, R., Moorwood, A. F. M., et al. 2002, A&A, 396, 439
Lyubenova, M., Kuntschner, H., & Silva, D. R. 2008, A&A, 485, 425
Lyubenova, M., van den Bosch, R. C. E., Côté, P., et al. 2013, MNRAS, 431, 3364
Maciejewski, W. 2004, MNRAS, 354, 892
Maciejewski, W., Teuben, P. J., Sparke, L. S., & Stone, J. M. 2002, MNRAS, 329, 502
Martini, P., Dicken, D., & Storchi-Bergmann, T. 2013, ApJ, 766, 121
Martini, P., Regan, M. W., Mulchaey, J. S., & Pogge, R. W. 2003, ApJ, 589, 774
Mazzalay, X., Rodríguez-Ardila, A., Komossa, S., & McGregor, P. J. 2013a, MNRAS, 430, 2411
Mazzalay, X., Saglia, R. P., Erwin, P., et al. 2013b, MNRAS, 428, 2389
Mihos, J. C., & Hernquist, L. 1994, ApJL, 431, L9
Miyoshi, M., Moran, J., Herrnstein, J., et al. 1995, Natur, 373, 127
Moorwood, A. F. M., & Oliva, E. 1990, A&A, 239, 78
Moorwood, A. F. M., & Oliva, E. 1994, ApJ, 429, 602
Müller-Sánchez, F., Prieto, M. A., Hicks, E. K. S., et al. 2011, ApJ, 739, 69
Oliva, E., Origlia, L., Kotilainen, J. K., & Moorwood, A. F. M. 1995, A&A, 301, 55
Peletier, R. F., Falcón-Barroso, J., Bacon, R., et al. 2007, MNRAS, 379, 445
Petitjean, P., & Durret, F. 1993, A&A, 277, 365
Phillips, M. M., & Malin, D. F. 1982, MNRAS, 199, 905
Pinkney, J., Gebhardt, K., Bender, R., et al. 2003, ApJ, 596, 903
Pogge, R. W. 1988, ApJ, 332, 702
Quillen, A. C., Alonso-Herrero, A., Rieke, M. J., et al. 1999, ApJ, 527, 696
Reid, M. J., Braatz, J. A., Condon, J. J., et al. 2009, ApJ, 695, 287
Reid, M. J., Braatz, J. A., Condon, J. J., et al. 2013, ApJ, 767, 154
Riffel, R., Riffel, R. A., Ferrari, F., & Storchi-Bergmann, T. 2011, MNRAS, 416, 493
Riffel, R., Rodríguez-Ardila, A., Aleman, I., et al. 2013a, MNRAS, 430, 2002
Riffel, R. A., & Storchi-Bergmann, T. 2011, MNRAS, 417, 2752
Riffel, R. A., Storchi-Bergmann, T., & Nagar, N. M. 2010, MNRAS, 404, 166
Riffel, R. A., Storchi-Bergmann, T., & Winge, C. 2013b, MNRAS, 430, 2249
Rigopoulou, D., Kunze, D., Lutz, D., Genzel, R., & Moorwood, A. F. M. 2002, A&A, 389, 374
Rodríguez-Ardila, A., Pastoriza, M. G., Viegas, S., Sigut, T. A. A., & Pradhan, A. K. 2004, A&A, 425, 457
Rodríguez-Ardila, A., Riffel, R., & Pastoriza, M. G. 2005, MNRAS, 364, 1041
Rush, B., Malkan, M. A., & Spinoglio, L. 1993, ApJS, 89, 1
Schmitt, H. R., Donley, J. L., Antonucci, R. R. J., Hutchings, J. B., & Kinney, A. L. 2003, ApJS, 148, 327
Seth, A. C. 2010, ApJ, 725, 670
Shlosman, I., Begelman, M. C., & Frank, J. 1990, Natur, 345, 679
Simões Lopes, R. D., Storchi-Bergmann, T., de Fátima Saraiva, M., & Martini, P. 2007, ApJ, 655, 718
Sosa-Brito, R. M., Tacconi-Garman, L. E., Lehnert, M. D., & Gallimore, J. F. 2001, ApJS, 136, 61
Stoklasová, I., Ferruit, P., Emsellem, E., et al. 2009, A&A, 500, 1287
Stone, J. L., Jr., Wilson, A. S., & Ward, M. J. 1988, ApJ, 330, 105
Storchi-Bergmann, T., Dors, O. L., Jr., Riffel, R. A., et al. 2007, ApJ, 670, 959
Storchi-Bergmann, T., Lopes, R. D. S., McGregor, P. J., et al. 2010, MNRAS, 402, 819
Storchi-Bergmann, T., McGregor, P. J., Riffel, R. A., et al. 2009, MNRAS, 394, 1148
Sun, A.-L., Greene, J. E., Impellizzeri, C. M. V., et al. 2013, ApJ, 778, 47
Takano, S., & Koyama, K. 1991, PASJ, 43, 1
Thean, A., Pedlar, A., Kukula, M. J., Baum, S. A., & O'Dea, C. P. 2000, MNRAS, 314, 573
Tueller, J., Baumgartner, W. H., Markwardt, C. B., et al. 2010, ApJS, 186, 378
van Dam, M. A., Bouchez, A. H., Le Mignant, D., et al. 2006, PASP, 118, 310
van de Ven, G., & Fathi, K. 2010, ApJ, 723, 767
van der Marel, R. P., & Franx, M. 1993, ApJ, 407, 525
Vasudevan, R. V., Brandt, W. N., Mushotzky, R., et al. 2013, ApJ, 763, 111
Vasudevan, R. V., Mushotzky, R. F., Winter, L. M., & Fabian, A. C. 2009, MNRAS, 399, 1553
Veilleux, S., Bland-Hawthorn, J., & Cecil, G. 1999a, AJ, 118, 2108
Veilleux, S., Bland-Hawthorn, J., Cecil, G., Tully, R. B., & Miller, S. T. 1999b, ApJ, 520, 111
Veilleux, S., Goodrich, R. W., & Hill, G. J. 1997, ApJ, 477, 631
Wallace, L., & Hinkle, K. 1996, ApJS, 107, 312
Walsh, J. L., van den Bosch, R. C. E., Barth, A. J., & Sarzi, M. 2012, ApJ, 753, 79
Winge, C., Storchi-Bergmann, T., Ward, M. J., & Wilson, A. S. 2000, MNRAS, 316, 1
Wizinowich, P. L., Le Mignant, D., Bouchez, A. H., et al. 2006, PASP, 118, 297
Yasuda, N., Fukugita, M., & Okamura, S. 1997, ApJS, 108, 417